

# Velocity-Structure Imaging Based on Seismological Observations Close to Hydraulic Fracturing Sites near Dawson Creek, Northeastern British Columbia (Parts of NTS 093P, 094A)

M.P. Roth<sup>1</sup>, Ruhr University Bochum, Germany, marco.roth@rub.de

R.M. Harrington, Ruhr University Bochum, Germany

Y. Liu, McGill University, Montréal, Quebec

Roth, M.P., Harrington, R.M. and Liu, Y. (2020): Velocity-structure imaging based on seismological observations close to hydraulic fracturing sites near Dawson Creek, northeastern British Columbia (parts of NTS 093P, 094A); *in* Geoscience BC Summary of Activities 2019: Energy and Water, Geoscience BC, Report 2020-02, p. 33–40.

## Introduction

Hydraulic-fracturing (HF) operations for hydrocarbon exploration have been associated with an increasing number of induced earthquakes in North America in the last decade (e.g., Ellsworth, 2013; Atkinson et al., 2016). In contrast to induced earthquakes in the United States being attributed to the high volume of co-produced wastewater being injected, induced earthquakes in the Western Canada Sedimentary Basin (WCSB) are often attributed to the HF operations themselves (e.g., Atkinson et al., 2016; Mahani et al., 2017). Although the majority of induced earthquakes are beneath the threshold to be felt (Ellsworth, 2013), some recent events exceeded a magnitude of  $M_4+$ , including an  $M_W$  4.6 on 17-Aug-2015 near Fort St. John (Mahani et al., 2017) and an  $M_L$  4.5 on 30-Nov-2018 near Dawson Creek (Mahani et al., 2019).

This paper focuses on the fluid migration after a single HF operation to investigate the role of pore-pressure increase as a potential source of induced earthquakes (Ellsworth, 2013). Double-difference-based tomography inversion and an earthquake sequence close to Dawson Creek in January 2019 were chosen to image fluid accumulation. This sequence is characterized by 190 earthquakes (Figure 1, red circles), detected on 15 stations with hypocentral distances between 5 and 50 km (Figure 1). The station network includes nine broadband stations operated by McGill University (Figure 1, blue triangles) and six broadband stations operated by the Pacific Geoscience Centre of the Geological Survey of Canada (PGC), two of which (NBC4, NBC7) are permanent stations (Figure 1, brown triangles). Green circles show all events detected with this station network, beginning in June 2017 (Figure 1).

## Methods

This study was based on seismological observations taken between 04-Jan-2019 and 11-Jan-2019 in a localized area close to an HF well (Figure 1, turquoise diamond), which was operating during this time period. Injection parameters provided by the British Columbia Oil and Gas Commission (BCOGC; last assessed on August 10, 2019) show a total injected volume of  $\sim 26\,000\text{ m}^3$  of fluids among all horizontal wells (Figure 1, turquoise lines) at the hypocentral depths of most of the seismicity. Fluid accumulation was investigated using a double-difference-tomography approach, based on differential arrival times calculated by cross-correlation lag times to invert for a 3D distribution of seismic P- to S-wave speed ratio ( $v_p/v_s$ ).

### Impact of Fluids on the $v_p/v_s$ Ratio

Areas of fluid accumulation were detected using an approach based on seismological observations, which derives from the impacts of fluids on the velocities of both body waves (i.e., compressional [P] and shear [S]). Inversion was carried out for the velocity of both types of wave, followed by calculation of their ratio.

The compressional-wave velocity ( $v_p$ ), which moves along the direction of propagation, is characterized by

$$v_p = [(\lambda + 2\mu)/\rho]^{1/2} = [(K + 4\mu/3)/\rho]^{1/2}, \quad (1)$$

and is thus dependent on the Lamé's constant ( $\lambda$ ), the rigidity ( $\mu$ ), the rock density ( $\rho$ ) and, alternatively, the bulk modulus ( $K$ ). Unlike the compressional wave, the shear-wave velocity ( $v_s$ ), which produces a displacement perpendicular to the direction of propagation, is defined by

$$v_s = (\mu/\rho)^{1/2}. \quad (2)$$

Thereby, the presence of fluids plays a role in influencing the velocities. On one hand, the mere substitution of non-filled cavities (i.e., porosity) with a fluid of higher density, such as water, will increase  $v_p$  while  $v_s$  stays rather constant as the bulk modulus increases, whereas the shear modulus

<sup>1</sup>The lead author is a 2019 Geoscience BC Scholarship recipient.

This publication is also available, free of charge, as colour digital files in Adobe Acrobat® PDF format from the Geoscience BC website: <http://www.geosciencebc.com/s/SummaryofActivities.asp>.

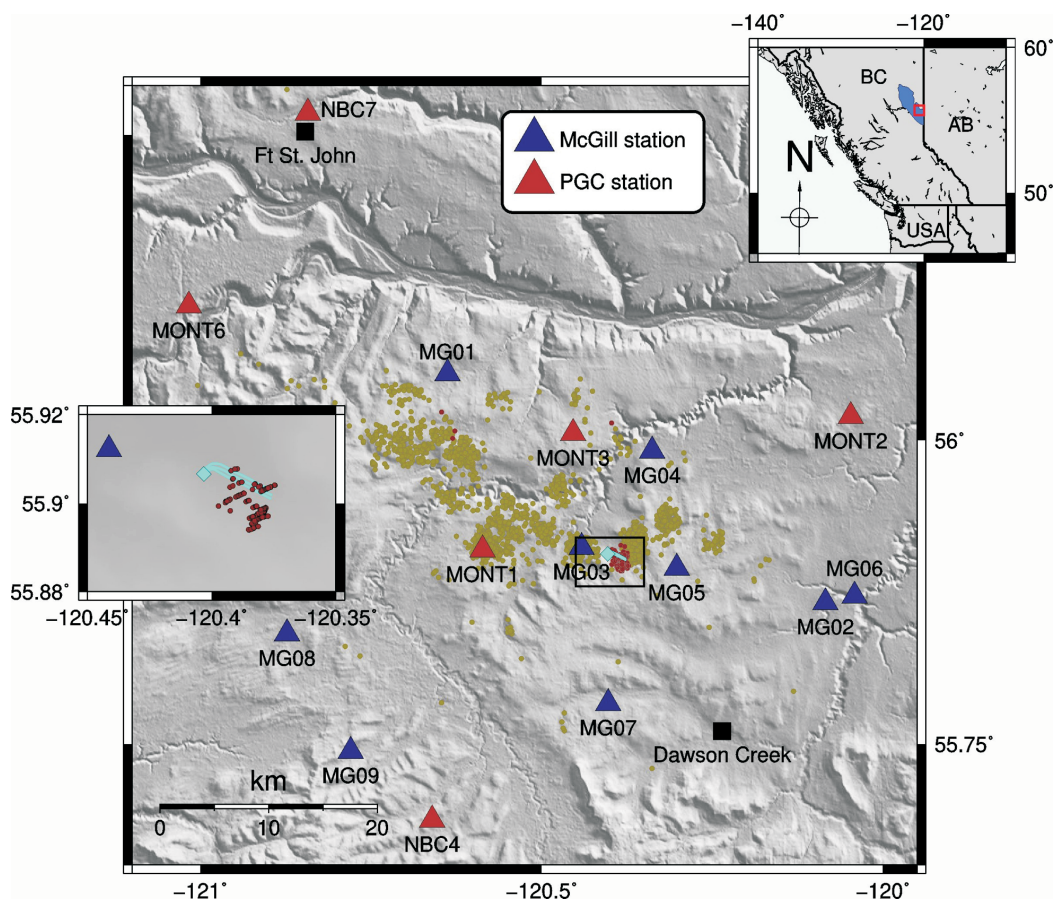


**Figure 1.** Study area in northeastern of British Columbia. McGill and PGC stations are denoted by blue and orange triangles, respectively. All detected earthquakes between 01-Jul-2017 and 11-Jan-2019 are shown as green dots, while the sequence of interest is highlighted in red. The HF well operating in the same time period as seismicity occurred is shown as a turquoise diamond. The inset map highlights the relative relocations of the chosen sequence.

remains constant (Han and Batzle, 2004). On the other hand, an increase in pore pressure at a constant confining pressure will decrease the seismic velocities significantly. This effect is even stronger on the shear-wave velocity (Christensen, 1984). This being said, zones of high  $v_p/v_s$  ratio possibly indicate high pore-fluid pressures (i.e., fluid accumulations along pre-existing faults or fractures due to pumping; Shelly et al., 2006).

### Double-Difference Tomography

Seismic tomography describes the process of imaging the subsurface of the Earth with the help of seismic waves (i.e., earthquakes of every kind). By using measured travel times and calculated ray paths, one creates an inverse problem, looking for a velocity model. Zhang and Thurber (2003) developed the seismic-tomography method ‘tomoDD’ based on double differences (Waldhauser and Ellsworth, 2000) to solve for this velocity model. The tomoDD software minimizes the misfit between observed and predicted arrival times, which are linearly related to the perturbations in the hypocentre and velocity-structure parameters, by applying the LSQR algorithm (Paige and Saunders, 1982) to

the least-square problem (Zhang and Thurber, 2003). The predicted travel times are calculated with a pseudo-bending raytracing algorithm (Um and Thurber, 1987).

This study employs this approach on an earthquake sequence close by Dawson Creek, presumably induced by hydraulic fracturing, that occurred between 04-Jan-2019 and 11-Jan-2019. During this time period, 190 events were detected using an STA/LTA approach with a dense array of 15 broadband stations at hypocentral distances of 5 to 50 km (Figure 1). The velocity inversion is based on a 1-D homogeneous layered velocity model based on Crust1.0 (Laske et al., 2013) for depth shallower than 1 km and on Mahani et al. (2017) for the deeper layers (Figure 2).

### Grid-Size Estimation and Quality Control

Resolution of the determined velocity structures is dependent on the initial grid spacing. A localized area (i.e.,  $5 \times 5 \text{ km}^2$  from the earthquake cluster centroid) was considered in this study, so the velocity grid spacing was in the order of hundreds of metres and was based on the minimum size of ground perturbations that cause changes in the

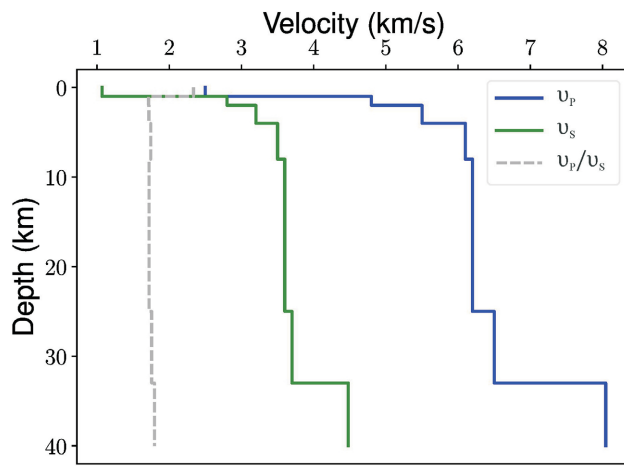


**Figure 2.** Homogeneous layered, 1-D velocity model, based on Crust1.0 for depth shallower than 1 km and Mahani et al. (2017) for deeper layers. The blue and green lines indicate P- and S-wave velocity, respectively. The grey dashed line shows the  $v_p/v_s$  ratio.

waveform. As an estimate, the grid spacing was calculated based on the maximum radius of the first Fresnel zone

$$b_{\max} = \frac{\sqrt{\lambda D}}{2}, \quad (3)$$

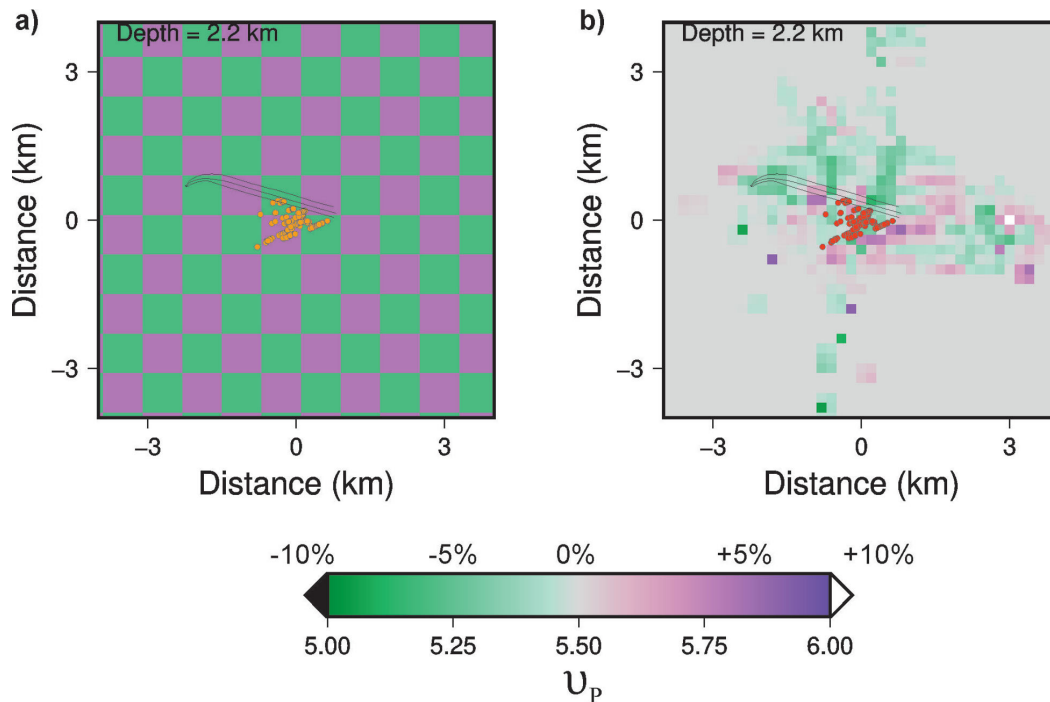
with wavelength ( $\lambda$ ) ranging from 10 to 30 m and signal-station distance of 5 to 50 km. With this approach, the minimum size of structures influencing the recorded waveforms lies between 100 and 600 m. The starting point was a horizontal grid spacing of 200 m to stay in the estimated range. To evaluate the reliability of the results, a checkerboard test (Figure 3) was carried out and the derivative-weight sum

(DWS), which quantifies the ray-path density around each grid point, was plotted from the real-velocity inversion (Figure 4). A checkerboard input model was created, with velocities changing by  $\pm 10\%$  of the initial velocity model (Figure 2), and  $600 \times 600$  m structures were generated (Figure 3a). The P-wave (Figure 4a) and S-wave (Figure 4b) arrivals were differentiated for the DWS distribution.

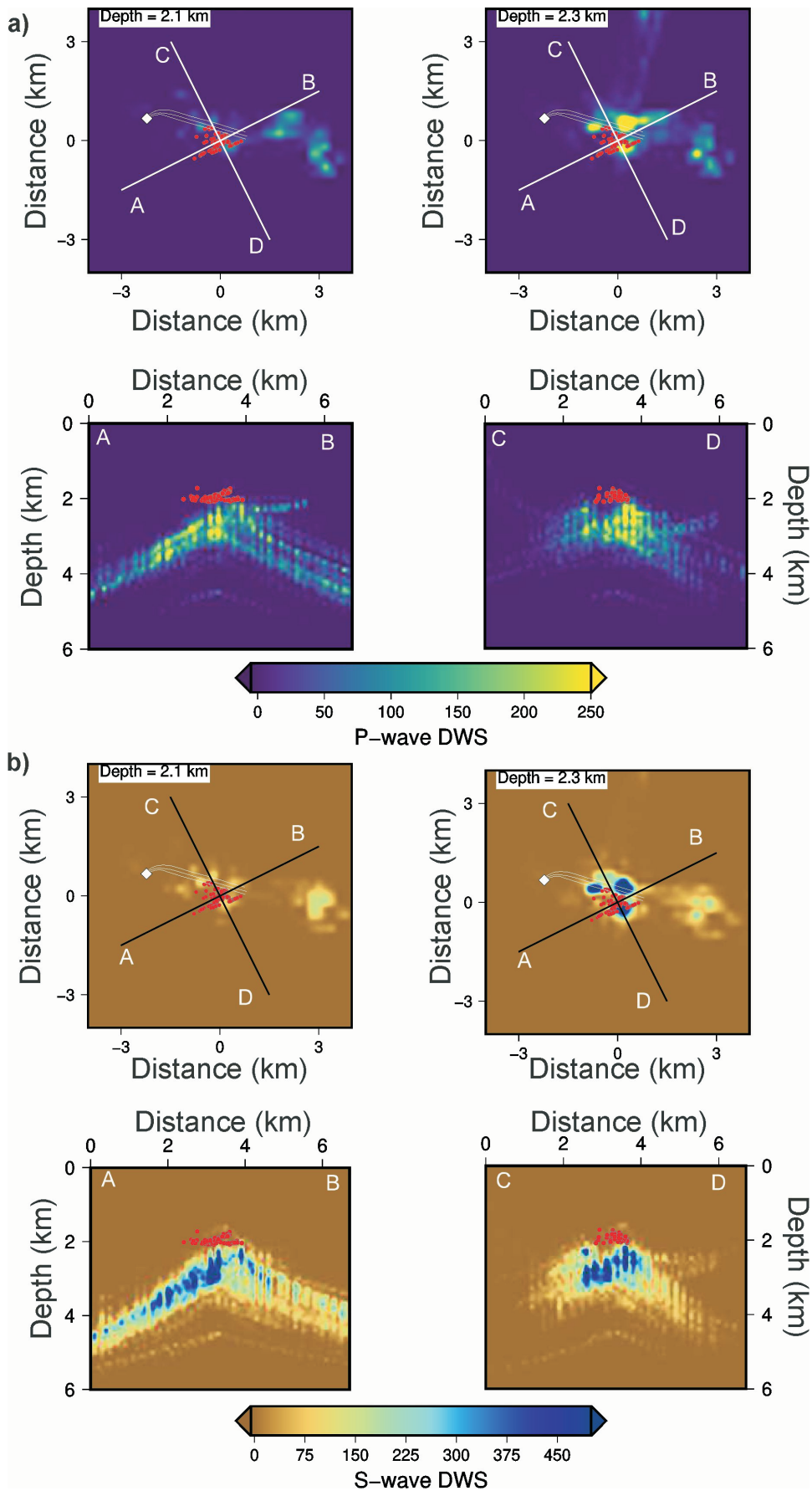
### Velocity-Structure Imaging

Similar to hypoDD by Waldhauser (2001), tomoDD uses initial locations combined with cross-correlation time shifts between different events observed at the same station as double-difference equations. In addition, tomoDD uses absolute travel-time data for the calculation of the ray paths. Cross-correlations in the present study are based on 2.5 s long recordings, starting 1 s before pick arrival time and ending 1.5 s after pick arrival time, with a bandpass filter between 2 and 15 Hz applied. Only event pairs that exceeded a threshold of a cross-correlation coefficient of 0.6 were used and the cross-correlation coefficient was used as a weighting factor. Iteration was carried out ten times using cross-correlation data only. The velocity-model joint inversion was applied in every second iteration step to already relocated event pairs.

The resulting  $v_p/v_s$  ratios were calculated at a depth corresponding with the horizontal wells and plotted in map view in Figure 5a–d. Figure 5e–f shows cross-sections along the profiles in Figure 5a–d, with one parallel and one perpen-



**Figure 3.** Checkerboard test of **a)** the input-velocity model with a synthetic checkerboard structure; and **b)** the results of the joint inversion based on the synthetic input from (a). Green and purple colours show zones of velocity decrease and increase by up to 10%, respectively.



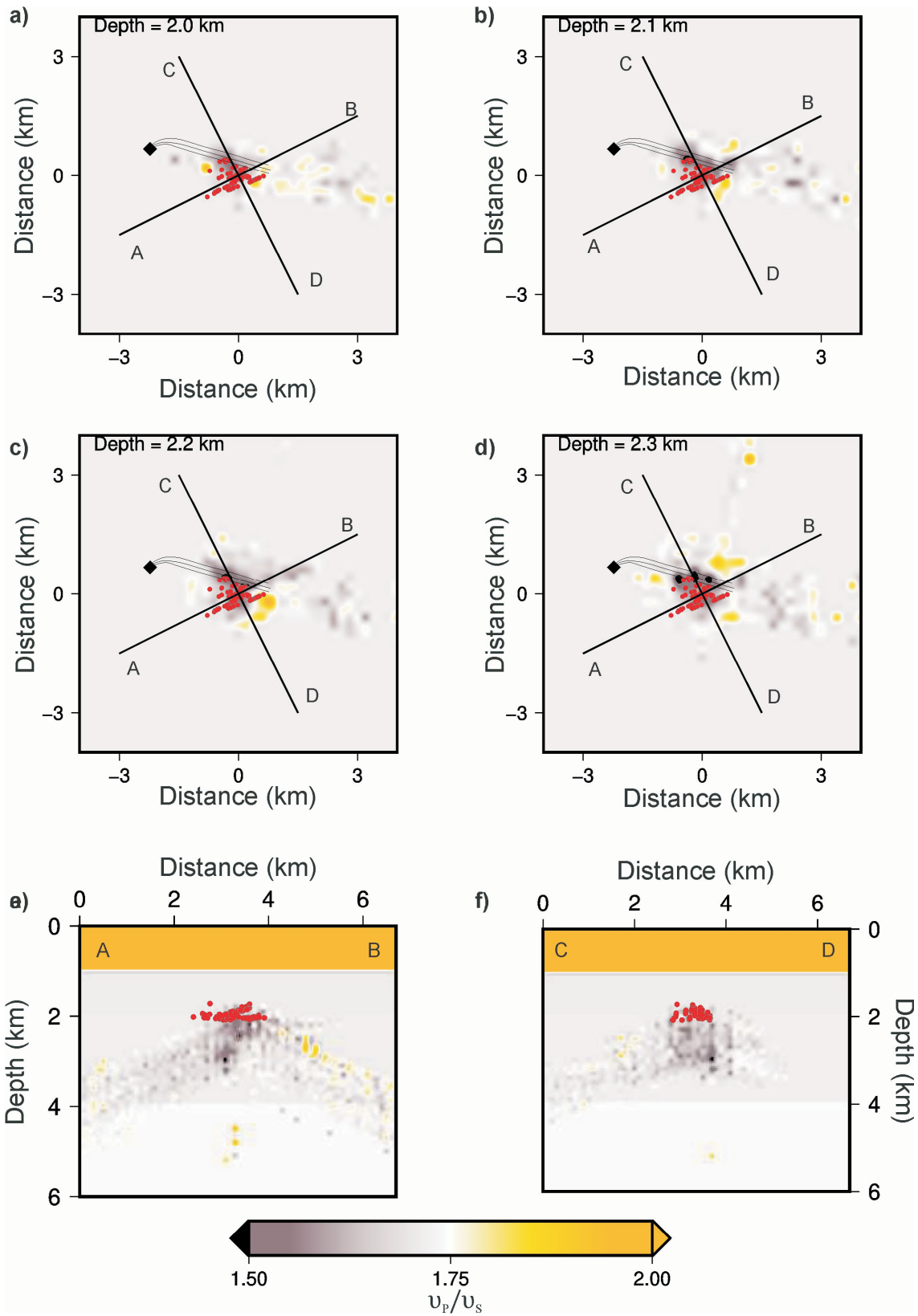


Figure 4. DWS plot of the velocity-structure inversion using the observed data, showing the results for a) P-wave arrival times, and b) S-wave arrival times.

Figure 5. Velocity-structure imaging based on seismicological observations taken between 04-Jan-2019 and 11-Jan-2019: a-d) map views at a depth of 2 to 2.3 km; e-f) cross-sections along profile lines shown in a-d.

dicular to the alignment of the events. Yellow colours indicate an increase in  $v_p/v_s$  ratio, while darker shades indicate a decrease.

## Results

The inset map in Figure 1 shows the relative relocations. The events align along several parallel northeast-trending structures. All event hypocentres are relocated in close proximity to horizontal wells.

Using the checkerboard test, it was possible to solve for velocity perturbations in the right order of magnitude: low-velocity zones with a decrease in velocity of 10% (Figure 3b; green shows a velocity of 5 km/h) and high-velocity zones with an increase in velocity of 10% (Figure 3b; purple shows a velocity of 6 km/h). The checkerboard test was not capable of spatially resolving the structure that was set in the input model (Figure 3).

The DWS distribution analysis in Figure 4 shows, for both P- and S-wave-based inversions, areas of more dense ray coverage very close to the centroid of hypocentres (~250 crossing ray paths per grid node with P-wave arrivals and 500 crossing ray paths per grid node with S-wave arrivals). No crossing ray paths were observed in the surrounding area.

Figure 5a–c shows changes in the  $v_p/v_s$  ratio in the direction of the horizontal well orientation, while Figure 5d shows also a perpendicular feature. Figure 5a suggests that patches of  $v_p/v_s$  increase along the horizontal well orientation, while Figure 5b–d shows, as well,  $v_p/v_s$  increase perpendicular to it. The cross-sections in Figure 5e–f show changes in  $v_p/v_s$  ratio concentrated deeper than the earthquake hypocentres, but the shape is dictated largely by the DWS distribution.

## Discussion and Conclusion

According to the quality-control criteria in Figures 3 and 4, there are limitations in applying the tomoDD software to the setting. On one hand, the checkerboard test (Figure 3) was able to image the amplitude of the velocity contrast from the input model but, on the other hand, the spatial distribution of structures that were given as an input has not been resolved. The plot of DWS values (Figure 4) shows limitations in the ray coverage, as the densest area covers only a radius of roughly 1 km around the events. Particularly the cross sections show that the DWS might image ray paths only from station MG03 to the west and station MG05 to the east.

Nevertheless, the observed increase in  $v_p/v_s$  ratio seems convincing with respect to the ambient stress field (i.e.,  $S_H$  striking  $43.7^\circ$  and  $S_H > S_h > S_v$ ; Bell and Grasby, 2012), as the fluids would follow structures along the horizontal

wells, perpendicular to  $S_H$ . This might indicate faults or zones of weakness along  $S_H$ . In addition, the small increases of  $v_p/v_s$  ratio parallel to  $S_H$  suggest a second orientation of fluid accumulations.

In conclusion, the tomoDD software was applied to an earthquake sequence in January 2019 to image fluid accumulations. Two possible fault orientations were observed: parallel and perpendicular to the largest principal stress. As the seismicity is occurring only in time windows of days and is very localized, the entire area is not well covered by ray paths, which limits the significance of these results.

## Acknowledgments

This project is partially funded by Deutsche Forschungsgemeinschaft (DFG) and Ruhr University Bochum (RUB) New Faculty Start-Up Funds. The authors acknowledge H. Kao and PGC, as well as G. Langston from McGill University, for help in station deployment; S. Venables and the BCOGC for providing well data; and K.D. Fischer from RUB Seismological Observatory for help in data acquisition and processing. The lead author received support through a Geoscience BC scholarship. A. Verdecchia provided a review that improved the quality of the manuscript.

## References

- Atkinson, G.M., Eaton, D.W., Ghofrani, H., Walker, D., Cheadle, B., Schultz, R., Shcherbakov, R., Tiampo, K., Gu, J., Harrington, R.M., Liu, Y., van der Baan, M. and Kao, H. (2016): Hydraulic fracturing and seismicity in the Western Canada Sedimentary Basin; *Seismological Research Letters*, v. 87, no. 3, p. 631–647.
- Bell, J.S. and Grasby, S.E. (2012): The stress regime of the Western Canadian Sedimentary Basin; *Geofluids*, v. 12, no. 2, p. 150–165.
- Christensen, N.I. (1984): Pore pressure and oceanic crustal seismic structure; *Geophysical Journal International*, v. 79, no. 2, p. 411–423.
- Ellsworth, W.L. (2013): Injection-induced earthquakes; *Science*, v. 341, no. 6142, p. 142.
- Han, D. and Batzle, M.L. (2004): Gassmann's equation and fluid-saturation effects on seismic velocities; *Geophysics*, v. 69, no. 2, p. 398–405.
- Laske, G., Masters, G., Ma, Z. and Pasyanos, M. (2013): Update on CRUST1.0 – a 1-degree global model of Earth's crust; *Geophysical Research Abstracts*, v. 15, EGU2013-2658.
- Mahani, A.B., Kao, H., Atkinson, G.M., Assaturians, K., Addo, K. and Liu, Y. (2019): Ground-motion characteristics of the 30 November 2018 injection-induced earthquake sequence in northeast British Columbia, Canada; *Seismological Research Letters*, v. 90, no. 4, p. 1457–1467.
- Mahani, A.B., Schultz, R., Kao, H., Walker, D., Johnson, J. and Salas, C. (2017): Fluid injection and seismic activity in the northern Montney play, British Columbia, Canada, with special reference to the 17 August 2015 Mw 4.6 induced earthquake; *Bulletin of the Seismological Society of America*, v. 107, no. 2, p. 542–552.

- Paige, C.C. and Saunders, M.A. (1982): LSQR: an algorithm for sparse linear equations and sparse least squares.; ACM Transactions on Mathematical Software (TOMS), v. 8, no. 1, p. 43–71.
- Shelly, D.R., Beroza, G.C., Ide S. and Nakamura, S. (2006): Low-frequency earthquakes in Shikoku, Japan, and their relationship to episodic tremor and slip; *Nature*, v. 442, p. 188–191.
- Um, J. and Thurber, C. (1987): A fast algorithm for two-point seismic ray tracing; *Bulletin of the Seismological Society of America*, v. 77, no. 3, p. 972–986.
- Waldhauser, F. (2001): hypoDD: a computer program to compute double-difference hypocenter locations; U.S. Geological Survey, Open File Report 01-113, p. 1–25.
- Waldhauser, F. and Ellsworth, W.L. (2000): A double-difference earthquake location algorithm: method and application to the northern Hayward fault, California; *Bulletin of the Seismological Society of America*, v. 90, no. 6, p. 1353–1368.
- Zhang, H. and Thurber, C.H. (2003): Double-difference tomography: the method and its application to the Hayward fault, California; *Bulletin of the Seismological Society of America*, v. 93, no. 5, p. 1875–1889.

